

# Impact of Fixing Spins in a Quantum Annealer with Energy Rescaling

Tomohiro Hattori<sup>1</sup>, Hiroataka Irie<sup>2</sup>, Tadashi Kadowaki<sup>2,3</sup> and Shu Tanaka<sup>1,4,5,6\*</sup>

<sup>1</sup> Graduate School of Science and Technology, Keio University, 3-14-1 Hiyoshi, Kohoku-ku, Yokohama-shi, Kanagawa 223-8522, Japan

<sup>2</sup> DENSO CORPORATION, Haneda Innovation City D3, 1-1-4, Hanedakuko, Ota-ku, Tokyo 144-0041, Japan

<sup>3</sup> National Institute of Advanced Industrial Science and Technology (AIST), 1-1-1, Umezono, Tsukuba-shi, Ibaraki 305-8568, Japan

<sup>4</sup> Department of Applied Physics and Physico-Informatics, Keio University, 3-14-1 Hiyoshi, Kohoku-ku, Yokohama-shi, Kanagawa 223-8522, Japan

<sup>5</sup> Keio University Sustainable Quantum Artificial Intelligence Center (KSQAIC), Keio University, Tokyo 108-8345, Japan

<sup>6</sup> Human Biology-Microbiome-Quantum Research Center (WPI-Bio2Q), Keio University, Tokyo 108-8345, Japan

Quantum annealing is a promising algorithm for solving combinatorial optimization problems. However, various hardware restrictions significantly impede its efficient performance. Size-reduction methods provide an effective approach for addressing large-scale problems but often introduce additional challenges. A notable hardware restriction is the limited number of decision variables quantum annealing can handle compared to the size of the problem. Moreover, when employing size-reduction methods, the interactions and local magnetic fields in the Ising model—used to represent the combinatorial optimization problem—can become excessively large, making them difficult to implement on hardware. Although prior studies suggest that energy rescaling impacts the performance of quantum annealing, its interplay with size-reduction methods remains unexplored. This study examines the relationship between fixing spins, a promising size-reduction method, and the effects of energy rescaling. Numerical simulations and experiments conducted on a quantum annealer demonstrate that the fixing spins method enhances quantum annealing performance while preserving the spin-chain embedding for a homogeneous, fully connected ferromagnetic Ising model.

## 1. Introduction

Combinatorial optimization problems are ubiquitous across various domains, necessitating high-accuracy solutions to address their complexity. A critical challenge in these problems is the exponential growth of solution candidates as the problem size increases. With the ongoing advancement of information-driven society, the demand for solving large-scale optimization problems has surged. Quantum annealing<sup>1–5)</sup> has emerged as a promising metaheuristic to effectively tackle these challenges.

Recently, quantum annealing has been applied across diverse fields, including logistics,<sup>6)</sup> materials science,<sup>7–9)</sup> and finance.<sup>10,11)</sup> Simultaneously, significant efforts have been devoted to developing and refining algorithms that leverage the potential of quantum annealing. This growing body of research underscores the importance of advancing quantum annealing methodologies for various combinatorial optimization applications.

Quantum annealing operates by searching for the ground state of the Ising model, which can be mapped to the solutions of combinatorial optimization problems. While many such problems can be formulated as Ising models, certain types, including those involving integer variables or black-box optimization, cannot be directly expressed in this framework. However, recent advancements are rapidly expanding the scope of quantum annealing, enabling it to address these complex problems.<sup>9,12–17)</sup> Furthermore, hybrid approaches that incorporate quantum annealers into intermediate stages of algorithms are broadening their applicability.<sup>18,19)</sup>

Despite these advancements, significant challenges remain in optimizing hardware for quantum annealing. These challenges can be categorized into three primary constraints: size restrictions, graph structure restrictions, and energy-scale restrictions.

Size restrictions are a critical barrier, limiting quantum annealers' ability to solve large-scale problems. Presently, the size of solvable problems is restricted by the number of qubits available on quantum annealing devices. As problem sizes grow, maintaining solution quality necessitates considerably longer annealing times.<sup>20,21)</sup> Additionally, decoherence effects increasingly hinder the performance of quantum annealers over extended durations, further complicating efforts to address large-scale optimization problems effectively.

Various methods have been proposed to mitigate the hardware size restrictions of quantum annealers, particularly through size-reduction techniques aimed at solving large-scale problems. One study introduced an approach to efficiently search for solutions to large-scale combinatorial optimization problems by classifying spins based on their convergence behavior in molecular dynamics simulations.<sup>22)</sup> Spins exhibiting slow convergence are deemed challenging to resolve and are delegated to quantum annealing for determination.

Other methods leverage sample persistence,<sup>23–26)</sup> which originates from the concept of persistency.<sup>27)</sup> Persistency involves rigorously solving specific quadratic pseudo-functions. However, solving a broad range of combinatorial optimization problems remains difficult. Classical methods assume that spins maintaining the same orientation after multiple iterations are likely to persist. These strategies enable quan-

\*shu.tanaka@appi.keio.ac.jp

tum annealers to address large-scale problems and produce high-quality solutions in practice. Nevertheless, the precise methodologies for resizing problems lack clarity, underscoring the importance of investigating the effects of problem size reduction.

In addition to size restrictions, the hardware limitations associated with graph structures in quantum annealers contribute to suboptimal solutions. Ising models with denser graphs than those supported by the quantum annealer's architecture cannot be faithfully represented. To bridge this gap, embedding methods have been developed.<sup>28,29)</sup> These techniques utilize qubit copies, referred to as *spin chains*, to effectively represent the couplers of dense Ising models. While such embeddings allow quantum annealers to handle dense graphs, they require a significant number of qubits and demand careful parameter tuning, particularly the *chain strength* between qubit copies. Setting optimal parameters is a challenging task, making embedding one of the factors that can compromise solution quality.

The second approach seeks to minimize the embedding overhead by reducing the problem size. In dense graph scenarios, the number of required couplings grows significantly with the number of spins. For instance, a fully connected graph with  $n$  spins requires  $n - 1$  couplings, demanding graph structures with higher connectivity as the number of spins increases.

The third approach involves error mitigation techniques. Previous studies have explored methods to relax errors and maintain solution accuracy by parallelizing the graph structure.<sup>30–33)</sup> Collectively, these approaches demonstrate diverse strategies to address the graph structure constraints of quantum annealers. Rescaling techniques are employed to embed the Ising model onto a practical quantum annealer, overcoming limitations related to energy scales. Recent studies suggest that energy rescaling impacts noise strength.<sup>34)</sup> Leveraging this property, researchers have estimated ideal energy parameters using zero-noise extrapolation. Another study treated rescaling parameters as variational parameters, showing that optimized rescaling significantly enhances performance.<sup>35)</sup> Therefore, incorporating rescaling considerations is essential for achieving high-quality solutions.

In this study, we explore the interplay between size-reduction techniques and rescaling techniques. Implementing size-reduction methods modifies the Ising model's properties, often resulting in large local magnetic field values. This alteration is closely linked to energy rescaling, highlighting the need to investigate their relationship comprehensively.

The remainder of this paper is structured as follows. Section 2 details the variable fixing and rescaling methods used in this study and outlines the problem setup. Section 3 presents the results for the homogeneous, fully connected ferromagnetic Ising model. Finally, Section 4 summarizes the findings and discusses potential future directions.

## 2. Setup

In quantum annealing, solutions to a combinatorial optimization problem are obtained by mapping them to the ground state of the Ising model. The Hamiltonian of the Ising model, representing the problem to be solved, is denoted as  $\mathcal{H}_p$ . Quantum fluctuations, which facilitate the exploration of the solution space, are represented by the driver Hamiltonian

$\mathcal{H}_d$ . The total Hamiltonian governing the quantum annealing process is expressed as:

$$\mathcal{H}(s) = A(s)\mathcal{H}_d + B(s)\mathcal{H}_p, \quad 0 \leq s \leq 1. \quad (1)$$

Here,  $s \in [0, 1]$  denotes the normalized time, where the annealing time  $\tau$  relates to the normalized time as  $s = \frac{t}{\tau}$ , with  $t$  being the elapsed time.

The quantum state is expected to adiabatically follow the ground state of the time-dependent Hamiltonian  $\mathcal{H}(t)$ , ultimately reaching the ground state of the Ising model at the final annealing time. According to the adiabatic theorem,<sup>36)</sup> the annealing time must be sufficiently long to ensure adiabatic evolution, which is determined by the minimum energy gap  $\Delta_{\min}$  between the ground state and the first excited state during the process. Consequently,  $\Delta_{\min}$  serves as a critical performance metric for quantum annealing.

In this study, transverse local magnetic fields are employed as the driver Hamiltonian as  $\mathcal{H}_d$ . The problem Hamiltonian  $\mathcal{H}_p$  and the driver Hamiltonian  $\mathcal{H}_d$  are expressed as follows:

$$\mathcal{H}_p = - \sum_{i=1}^N h_i \sigma_i^z - \sum_{1 \leq i < j \leq N} J_{ij} \sigma_i^z \sigma_j^z, \quad (2)$$

$$\mathcal{H}_d = - \sum_{i=1}^N \sigma_i^x, \quad (3)$$

where  $N$  represents the number of spins,  $h_i$  represents the local magnetic field acting on the  $i$ th spin,  $J_{ij}$  represents the interaction between the  $i$ th and  $j$ th spins, and  $\sigma_i^x, \sigma_i^z$  are Pauli matrices associated with the  $i$ -th spin component.

Upon applying the fixing spins method, the Hamiltonians are modified. The following explains the fixing spin method, in which some spin variables are fixed at  $+1$  or  $-1$ . The updated problem Hamiltonian,  $\mathcal{H}'_p$ , and the driver Hamiltonian,  $\mathcal{H}'_d$ , after fixing spins are given as follows:

$$\mathcal{H}'_p = - \sum_{i'=1}^n h'_{i'} \sigma_{i'}^z - \sum_{1 \leq i' < j' \leq n} J'_{i'j'} \sigma_{i'}^z \sigma_{j'}^z, \quad (4)$$

$$\mathcal{H}'_d = - \sum_{i'=1}^n \sigma_{i'}^x, \quad (5)$$

where  $n$  denotes the number of spins after applying the fixing spins method, and  $i', j' (= 1, \dots, n)$  are the indices corresponding to the spins after fixing spins. The parameters  $h'_{i'}$  and  $J'_{i'j'}$  are expressed as follows:

$$h'_{i'} = h_{i'} + \sum_{k'=n+1}^N J_{i'k'} s_{k'}, \quad (6)$$

$$J'_{i'j'} = J_{i'j'}, \quad (7)$$

where  $s_k = \pm 1$  represents the fixed spin. As shown in Eq. (6) and Eq. (7), the interaction terms involving fixed spins reduce to local magnetic fields, while the interaction terms not connected to the fixed spins remain unchanged. Figure 1 illustrates the conceptual diagram of fixing spins in a fully connected Ising model with  $N = 6$ . The local magnetic field terms at fixed spins and the interaction terms between fixed spins become constants, meaning they do not contribute to the reduced problem. Additionally, the interaction terms between a fixed spin and a spin in the reduced problem transform into

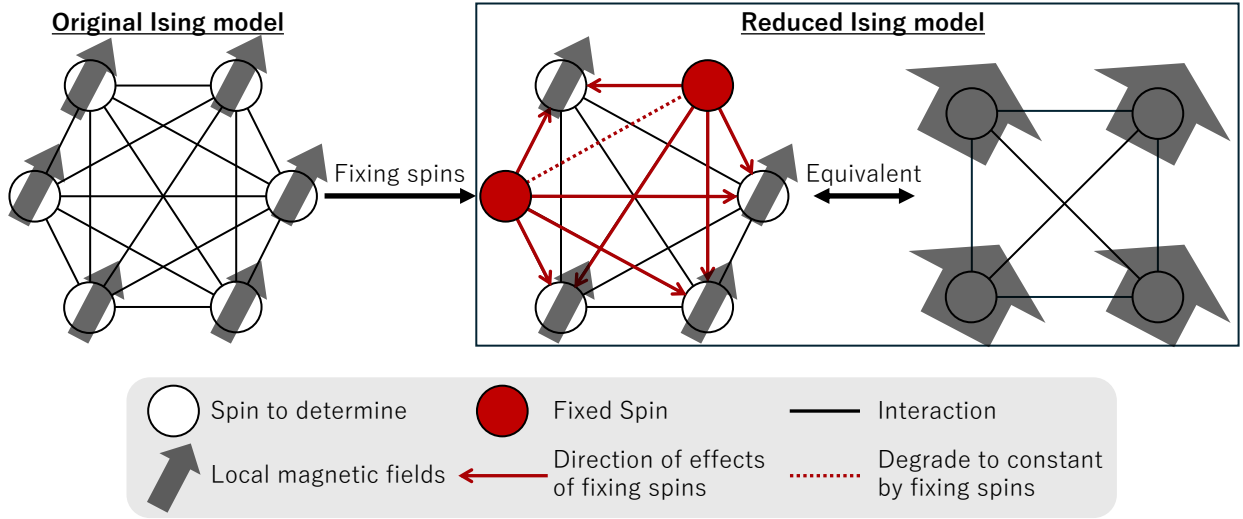


**Fig. 1.** (Color online) Conceptual diagram illustrating the fixing spins method. This method reduces the size of the Ising model while altering the properties of local magnetic fields. The graph on the left represents the original Ising model, where white circles indicate spins determined by quantum annealing, and red circles represent fixed spins. Black arrows denote the local magnetic fields at each vertex, while solid lines indicate the interactions of the Ising model. The dotted line represents an interaction that simplifies to a constant due to the fixed spins. Dark red arrows illustrate the directional effects of the fixed spins on the system. The graph on the right depicts the reduced Ising model, where the influence of the fixed spins enhances the local magnetic fields of the simplified problem. In this instance, a fully connected Ising model with  $N = 6$  is reduced to a fully connected Ising model with  $N = 4$ .

local magnetic fields. Therefore, the effects of fixing spins are twofold: reducing the number of spins and altering the properties of the local magnetic fields.

The selection of spins to be fixed, along with their respective directions, is determined using a classical pre-processing method from previous studies.<sup>22–26</sup> In this study, to characterize the fixed spins without assuming a predetermined selection, we adopt the error probability  $p_{\text{err}}$  as defined in the previous study.<sup>21</sup> The error probability  $p_{\text{err}}$  is the proportion of spins that are aligned with the direction of the ground state of the Ising model within the spin configuration. The previous study shows the effectiveness of fixing spins for large-scale combinatorial optimization problems in quantum annealer. Also, fixing spin method enhance the performance of the quantum annealing from the perspective of energy gap. However, the impact of the error of fixing spins on the energy gap are not revealed.

The input parameter ranges for hardware are defined as  $[M_{\min}, M_{\max}]$  for the local magnetic field and  $[\mathcal{J}_{\min}, \mathcal{J}_{\max}]$  for the interaction. These parameters  $h_i$  and  $J_{ij}$  are rescaled to fit within these ranges by dividing by the rescaling parameter  $r$ . In the previous study,<sup>21</sup> the rescaling parameter  $r$  is defined as follows:

$$r = \max \left\{ \frac{\max\{h_i\}}{M_{\max}}, \frac{\min\{h_i\}}{M_{\min}}, \frac{\max\{J_{ij}\}}{\mathcal{J}_{\max}}, \frac{\min\{J_{ij}\}}{\mathcal{J}_{\min}} \right\}. \quad (8)$$

In this study, the primary objective is to explore the effects of rescaling. To this end, we investigated the dependence of quantum annealing performance on the rescaling parameter  $r$ . The Hamiltonian after rescaling is expressed as follows:

$$\mathcal{H}_p'' = \frac{\mathcal{H}_p'}{r}. \quad (9)$$

The quantum annealing Hamiltonian after rescaling is ex-

pressed as follows:

$$\mathcal{H}'(t) = A(s)\mathcal{H}'_d + B(s)\mathcal{H}'_p''. \quad (10)$$

The rescaling parameters are affected by fixing spins because the interaction terms  $J_{ij}\sigma_i^z\sigma_j^z$  are transformed into  $J_{ik}\sigma_i^z s_k$ , which function as effective local magnetic fields, as shown in Eq. (6). Consequently, the fixing spins method alters the range of local magnetic fields, thereby influencing the rescaling parameters. This study examines the relationship between the fixing spins method and rescaling. A previous study<sup>21</sup> demonstrated performance improvements through fixing spins. However, this conclusion may not hold when rescaling is considered.

### 3. Results

In this study, for simplicity, we focus on a homogeneous fully connected ferromagnetic Ising model, as the Ising model obtained after fixing spins results in another fully connected Ising model. Thus, the model generated after fixing spins will not include isolated spins, making it easier to analyze.

The homogeneous fully connected ferromagnetic Ising model is expressed as follows:

$$\mathcal{H}_p = -h \sum_{i=1}^N \sigma_i^z - J/N \sum_{1 \leq i < j \leq N} \sigma_i^z \sigma_j^z. \quad (11)$$

The normalization by  $1/N$  ensures that  $\mathcal{H}_p$  is an extensive quantity. If the ground state is degenerate, determining the error rate becomes challenging because the Hamming distance from the ground state is not uniquely defined. Therefore, we consider the Ising model without degeneracy. The ferromagnetic Ising model with  $h = 0$  exhibits trivial twofold degeneracy. To eliminate this trivial degeneracy, we set  $h = 0.1$  and  $J = 1$ . The ground state of this homogeneous fully connected Ising model is trivially the all-up state.

The D-Wave Advantage system 6.4<sup>37</sup>) was used as the quantum annealer for the experiment. This system features

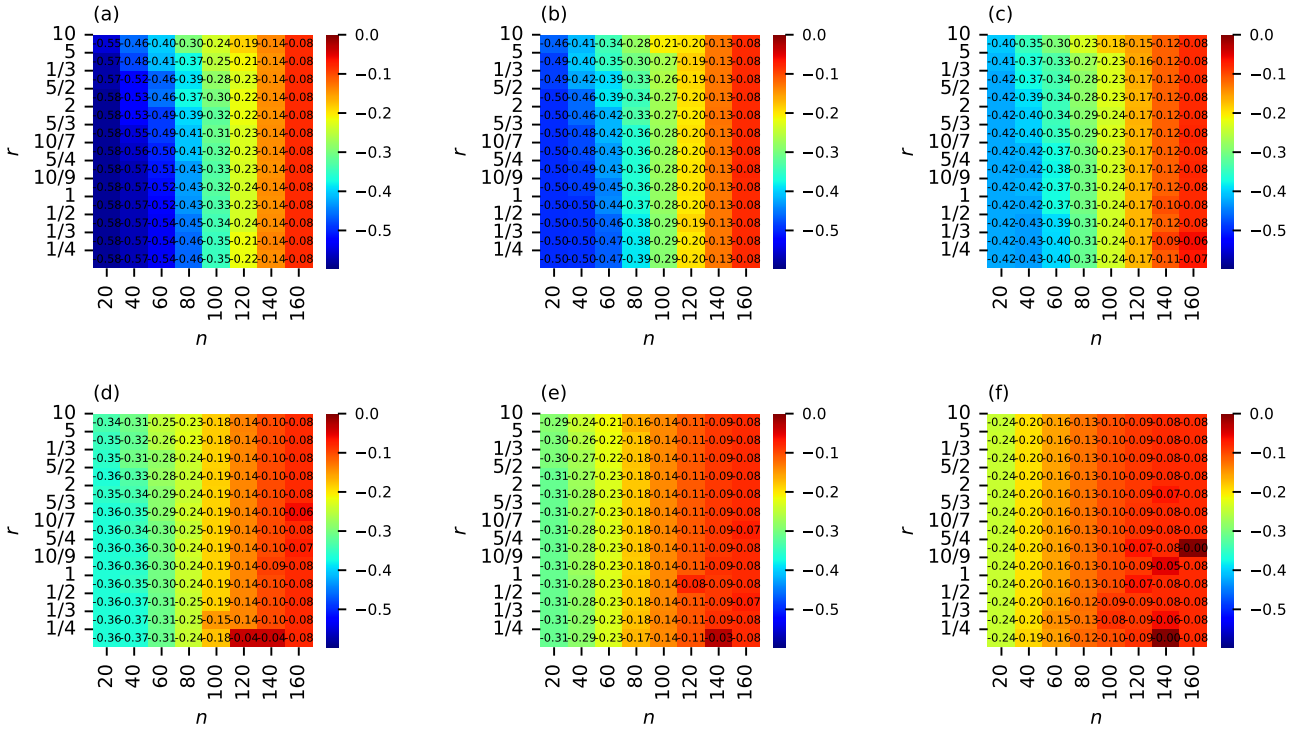


**Fig. 2.** (Color online) The color map shows the distribution of the minimum energy in the  $n$  versus  $r$  space for the homogeneous fully connected ferromagnetic Ising model with  $N = 160$ .  $n = 160$  corresponds to the results without fixed spins. The annealing time is set to  $\tau = 2000.0 \mu\text{s}$ . The ground state energy is 0.597. Each panel represents a different error rate for fixing spins, with  $p_{\text{err}}$  set to (a)  $p_{\text{err}} = 0.0$ , (b)  $p_{\text{err}} = 0.1$ , (c)  $p_{\text{err}} = 0.2$ , (d)  $p_{\text{err}} = 0.3$ , (e)  $p_{\text{err}} = 0.4$  and (f)  $p_{\text{err}} = 0.5$ , respectively.

5760 physical qubits arranged in the Pegasus graph,<sup>38)</sup> enabling the embedding of a complete graph with 177 logical qubits through minor embedding.<sup>28,29)</sup> However, not all qubits in the system are functional. Consequently, the number of spins in the Ising model was set to  $N = 160$ , the near maximum size that can be embedded in the quantum annealer.

The Ising model is embedded in the quantum annealer using minor embedding, and the chain strength—representing the interaction between physical qubits—must be adjusted to ensure that spins within the same spin chain align in the same direction. If the *auto-scale* method is employed,<sup>39)</sup> the chain strength increases with the length of the spin chain. As a result, the chain strength must remain within the range  $[\mathcal{J}_{\text{min}}, \mathcal{J}_{\text{max}}]$  for the interaction. For this study, the chain strength was set to the maximum value of 2.0, which is the strongest value permissible in this configuration.<sup>39)</sup>

The ground state search in the quantum annealer was performed 100 times due to the stochastic behavior of the system, and the minimum energy from these 100 runs was adopted as the energy output of the quantum annealer in this experiment.

Additionally, we investigated the energy gap using exact diagonalization for the same fully connected Ising model, without considering the embedding effect. The energy gap analysis yielded similar results for the long annealing time limit. Finally, we investigated the properties of the system at the thermodynamic limit, accounting for the effects of rescaling and fixing spins.

### 3.1 Experiment on an actual quantum annealer

When embedding an Ising model with a large energy scale into a real quantum annealer, rescaling the energy scale becomes unavoidable. This rescaling is performed as described in Eq. (8). The experiment was conducted on the D-Wave Advantage system 6.4 to examine the dependence of the quantum annealer's performance on the rescaling parameter.

Figure 2 illustrates the parameter dependence of the energy. Since the energy scale after rescaling differs from the pre-rescaling energy scale, the energy values are restored to the original Ising model, as expressed in Eq. (11), after solving them with the quantum annealer. The  $x$ -axis represents the number  $n$  of spins after fixing spins, and the  $y$ -axis denotes the rescaling parameter  $r$ , as shown in Eq. (9). As  $r$  decreases, the quantum annealer achieves lower energy, as shown in Fig 2 (a)-(c). This result indicates that a wide parameter range is necessary to maintain the performance of the quantum annealer.

Conversely, the dependence on  $r$  gradually diminishes in both high error probability scenarios and when the size of the reduced problem increases, as seen in Fig. 2. The behavior of the local magnetic fields in the reduced problems after fixing spins is consistent across these scenarios. Errors in fixing spins affect the local magnetic fields of the reduced problem. The upper bound of the absolute value of the local magnetic fields after fixing spins is given by:

$$h'_i = h_i + \sum_{k=n+1}^N J_{ik} S_k \leq h_i + \sum_{k=n+1}^N |J_{ik}|. \quad (12)$$

Eq. (12) exhibits the maximum increase in the range of the local magnetic field due to fixed spins. Since we are dealing with a homogeneous fully connected ferromagnetic Ising model, after fixing spins with  $p_{\text{err}} = 0$ , the local magnetic fields correspond to this upper bound, as shown in Eq. (12). When fixing spins with  $p_{\text{err}} = 0$ , the local magnetic fields change as follows:

$$h' = h + J(N - n) = h + \sum_{k=n+1}^N |J_k|. \quad (13)$$

Following Eq. (6), the homogeneous fully connected ferromagnetic Ising model after fixing spins with  $p_{\text{err}}$  is expressed as follows:

$$h' = h + J(N - n)(1 - 2p_{\text{err}}). \quad (14)$$

Equation (14) indicates that  $h'$  decreases as  $p_{\text{err}}$  and  $n$  increase. Consequently, the effects of rescaling become more pronounced when  $p_{\text{err}} = 0$ . According to Eq. (14),  $h'$  equals  $h$  when  $p_{\text{err}} = 0.5$  or  $n = N$ . In this case, the energy range of the Ising model remains unchanged. Therefore, fixing spins does not affect the energy range, and the dependence on  $r$  disappears.

High energy points observed in Fig. 2 (d)-(f) result from the breaking of the embedding chain in the hardware. The local magnetic field is distributed equally among the spins within the spin chain. Consequently, the local magnetic fields are weaker compared to before the spin chain was constructed. Consequently, a longer chain length requires a stronger chain strength to prevent chain breakage. As the number of spins increases, a stronger spin chain is needed to maintain its integrity. For a spin chain to remain intact when the chain strength is weak, the spins in the chain must have identical values, without the interaction effects between them.

Therefore, with a small  $h$ , it becomes increasingly difficult to maintain the spin chain as its length grows. Consequently, with large  $n$  and  $p_{\text{err}}$ , the spin chain is more likely to break compared to other parameter ranges. Additionally, because the Ising model parameters are extensive and the chain strength is relatively weak, the chain breaks more frequently when  $r$  is small. To prevent chain breakage, expanding the parameter range is necessary to accommodate large-scale problems when embedding into the quantum annealer. These results highlight the importance of fixing spins in the correct direction to achieve lower energy and preserve spin chains on the hardware.

### 3.2 Energy gap analysis

Since the minimum energy gap between the ground state and the first excited state,  $\Delta_{\text{min}}$ , reflects the performance of quantum annealing in the adiabatic limit, as per the adiabatic condition,<sup>36,40)</sup> we investigated its properties. Figure 3 shows  $\Delta_{\text{min}}$  of the Hamiltonian after fixing spins with  $p_{\text{err}} = 0$  and rescaling with  $r$ .

The number of fixing spins  $n$  at which  $\Delta_{\text{min}}$  is maximized varies for each  $r$  as shown in Fig. 3. Energy gap  $\Delta_{\text{min}}$  increases with  $n$ , consistent with a previous study.<sup>21)</sup> However, the fixing spins method does not necessarily lead to an expansion of  $\Delta_{\text{min}}$  when rescaling is considered. For example, when  $r = 5/2$ , the maximum  $\Delta_{\text{min}}$  occurs at  $n = 140$ . These results indicate a trade-off between the energy gap expansion

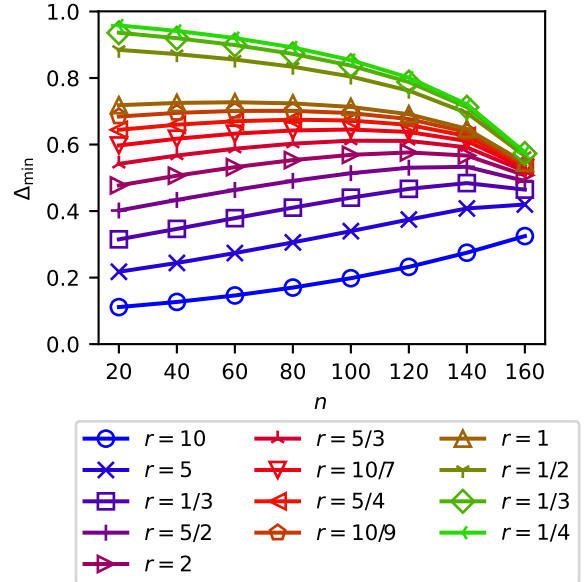


**Fig. 3.** (Color online) The minimum energy gap  $\Delta_{\text{min}}$  of the Hamiltonian after fixing spins with  $p_{\text{err}} = 0$  and rescaling with  $r$  for the homogeneous fully connected ferromagnetic Ising model with  $N = 160$ .  $n = 160$  corresponds to the results without fixing spins. Solid lines between points are provided as a guide to the eye.

due to fixing spins and the reduction of the energy gap caused by rescaling. Additionally, for  $r = 1/4$ ,  $\Delta_{\text{min}}$  decreases as  $n$  increases. This demonstrates that the effects of fixing spins depend on the rescaling parameter. The findings emphasize the importance of exploring the relationship between fixing spins and rescaling.

Next, we investigated the behavior of  $\Delta_{\text{min}}$ , including errors in fixing spins. Figure 4 presents a heatmap of  $\Delta_{\text{min}}$  for different values of  $r$  and  $n$ . Each panel corresponds to a different  $p_{\text{err}}$ . As shown in Figure 4, as  $p_{\text{err}}$  increases or  $r$  decreases, the optimal  $n$  that maximizes  $\Delta_{\text{min}}$  becomes smaller. These results suggest that both  $r$  and  $n$  must be carefully considered to achieve high-quality solutions. For  $r = 1.0$ , fixing spins (lower  $n$ ) improves  $\Delta_{\text{min}}$ . In contrast, for  $r = 10$ , fixing spins reduces  $\Delta_{\text{min}}$ . These findings highlight the necessity of considering the rescaling parameters when fixing spins and adjusting parameters accordingly. Fixing spins has a positive effect at small  $r$ , but a negative effect at large  $r$ .

We further investigated the energy gap in the thermodynamic limit using the analytical method from the previous study<sup>41)</sup> to assess the scalability of the numerical analysis. The details of the analytical method are provided in appendix A. According to this method, the model is expressed as a harmonic oscillator. The energy gap derived from the method is given by:

$$\Delta(s) = \left\{ s^2 \sin^2 \theta_0 \left( \frac{h}{r} + \frac{1 + \sin^2 \theta_0}{s \sin \theta} \right)^2 - \frac{(1 + \sin^2 \theta_0)^2}{s^2 \sin^2 \theta} \right. \\ \left. + s^2 \sin^4 \theta_0 \frac{J^2}{r^2} + s[2 \sin^2 \theta_0 - (1 - s) \cos^3 \theta_0] \frac{J}{r} \right. \\ \left. + (1 - s)^2 \cos^2 \theta_0 \right\}^{\frac{1}{2}}, \quad 0 \leq s \leq 1. \quad (15)$$

Figure 5 shows the magnetic process of  $\Delta_{\text{min}}$  in the thermo-

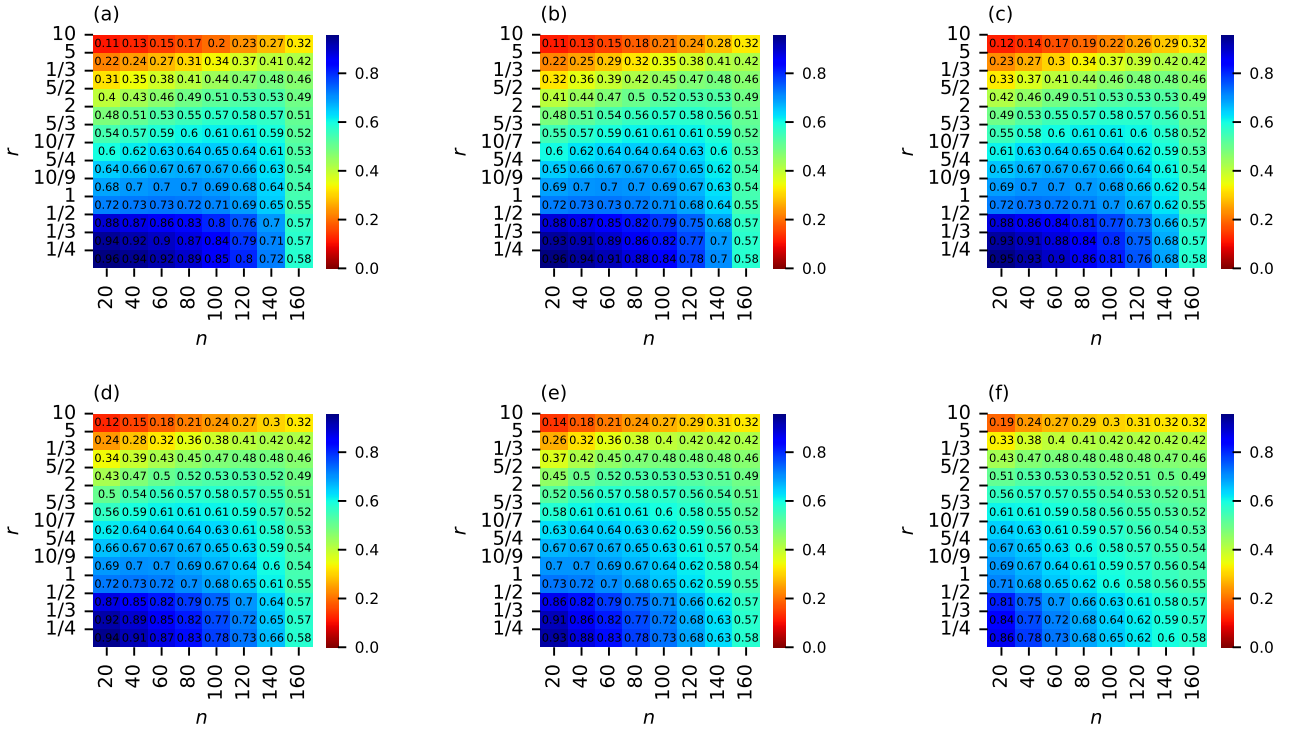


**Fig. 4.** (Color online) Color map of the minimum energy gap  $\Delta_{\min}$  distribution in  $n$  versus  $r$  space for the homogeneous fully connected ferromagnetic Ising model with  $N = 160$ .  $n = 160$  represents the results without fixing spins. Each panel corresponds to a different error rate  $p_{\text{err}}$  for fixing spins: (a)  $p_{\text{err}} = 0.0$ , (b)  $p_{\text{err}} = 0.1$ , (c)  $p_{\text{err}} = 0.2$ , (d)  $p_{\text{err}} = 0.3$ , (e)  $p_{\text{err}} = 0.4$ , (f)  $p_{\text{err}} = 0.5$ .

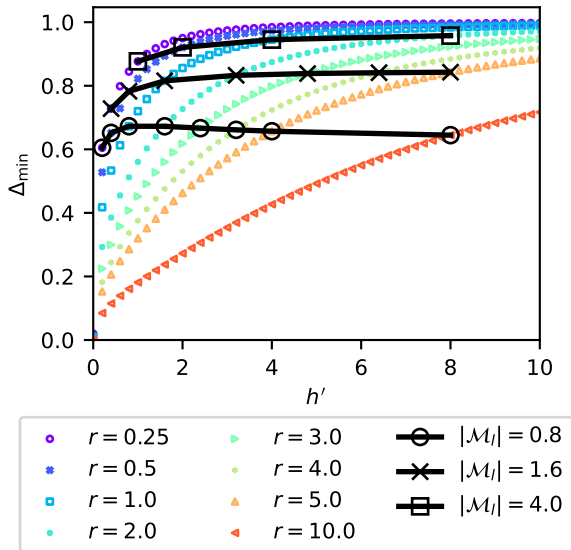


**Fig. 5.** (Color online) Minimum energy gap  $\Delta_{\min}$  at the thermodynamic limit for different  $h'$ . Black lines represent  $\Delta_{\min}$  for the same  $h$  range condition with different  $r$ . The assumption is that spins are fixed up to the maximum value where the local magnetic fields reach  $h/r$ . This comparison considers the same value of  $h/r$  across different numbers of spins but within the same parameter range. When  $r$  is small, the number of fixed spins is small, while for large  $r$ , the number of fixed spins increases.

dynamic limit, where the minimum energy gap with respect to  $s$  is denoted as  $\Delta_{\min}$  in Eq. (15). The fixing spins method introduces local magnetic fields without reducing the system size in the thermodynamic limit because the finite number of

fixed spins is negligible compared to the total number of spins in the system. Hence, increasing the local magnetic fields  $h'$  corresponds to increasing the number of fixed spins, which is related to a decrease in  $n$  in Eq. (14). The error rate in fixing spins is also reflected by the reduction in local magnetic fields, as described by Eq. (14).

In Fig. 5,  $\Delta_{\min}$  increases as  $r$  decreases, in line with the increase in the local magnetic fields  $h'$  after fixing spins. This indicates that smaller values of  $r$  are more favorable for quantum annealing, assuming no restrictions on the parameter range. The descending order of  $h'$  corresponds directly to the descending order of  $\Delta_{\min}$ . However, it is important to note that the allowed parameter range differs for each  $r$  in Fig. 5, even though the parameter range is constrained in actual hardware. Therefore, the comparison is more advantageous for settings with smaller  $r$ .

We also investigated  $\Delta_{\min}$  while considering the restrictions of the parameter range. The black lines in Fig. 5 illustrate a comparison of  $\Delta_{\min}$  within the same  $h$  range  $[\mathcal{M}_{\min}, \mathcal{M}_{\max}]$ , where we assume  $|\mathcal{M}_{\min}| = |\mathcal{M}_{\max}|$ . We focus solely on the  $h$  range because, in this numerical simulation, the  $h$  range is always broader than the  $J$  range after fixing spins. According to Fig. 5, the point at which the maximum energy gap occurs in the line of  $|\mathcal{M}_{\min}| = 0.08$  is at  $r = 1/2$ , while for the line of  $|\mathcal{M}_{\min}| = 0.8$ , it occurs at  $r = 1.0$ . These results suggest that optimal rescaling parameters exist for different  $h$  ranges. Therefore, the effects of fixing spins in the thermodynamic limit also depend on the rescaling parameter.

When the  $h$  range is wide, the fixing spins method is effective in expanding  $\Delta_{\min}$ . In contrast, when the  $h$  range is narrow, the fixing spins method becomes less effective because

the rescaling effects, which reduce  $\Delta_{\min}$ , dominate over the benefits of expanding  $\Delta_{\min}$  through fixing spins. These findings are also supported by the finite-size Ising model results in Fig. 4. The same considerations apply to the energy gap at finite sizes, even if the problem scale increases. Therefore, the properties of the energy gap with fixing spins and rescaling are extensive with respect to size.

#### 4. Conclusion

We investigated the effects of rescaling and fixing spins through both experimental hardware and numerical simulations. The experiment clarifies the impact of fixing spins and rescaling on a homogeneous fully connected ferromagnetic Ising model. Our results demonstrate that fixing spins effectively leads to a low energy state in quantum annealing hardware. Additionally, fixing spins preserves the spin chain generated by the minor embedding, which is an inherent feature when embedding the Ising model into hardware.

These findings suggest that the size-reduction method requires a broader range of parameters to address larger-scale problems on hardware. Furthermore, to solve large-scale problems effectively, a fixing spins method with a low error probability is essential. The results also emphasize that increasing the number of couplers for each qubit is a powerful strategy to prevent chain breaking, as avoiding long spin chains helps mitigate the chain strength issue.

Energy gap analysis provided insights into the adiabatic limit, as the energy gap reflects the properties of this limit. According to the numerical simulations, rescaling with a small parameter is not an effective way to increase the number of spins to fix. From the perspective of  $\Delta_{\min}$ , a trade-off exists between the positive effects of fixing spins and rescaling. The insight that a wider parameter range is necessary to overcome these issues aligns with the experimental results.

At the thermodynamic limit, this trade-off is also confirmed. In situations with the same parameter range, a larger energy gap is obtained as the number of fixing spins increases. These results are consistent with those observed in finite-size settings, indicating similar trends in larger-scale finite-size problems. The trade-off insight suggests that expanding both the parameter range and the number of couplers is as crucial as increasing the number of qubits.

This study investigated the simplest setup to explore the complex relationships between fixing spins and rescaling. Future work will involve investigating other models, such as the random Ising model and combinatorial optimization with constraints, which exhibit different properties of local magnetic fields that increase after fixing spins.

S. T. was supported in part JSPS KAKENHI (Grant Number JP21K03391) and JST Grant Number JPMJPF2221, the Council for Science, Technology, and Innovation (CSTI) through the Cross-ministerial Strategic Innovation Promotion Program (SIP), ‘‘Promoting the application of advanced quantum technology platforms to social issues’’ (Funding agency: QST). Human Biology-Microbiome-Quantum Research Center (Bio2Q) is supported by World Premier International Research Center Initiative (WPI), MEXT, Japan.

#### Appendix A: Energy-gap analysis by bosonization in thermodynamic limit

The total Hamiltonian with rescaling is written as follows:

$$\begin{aligned}\mathcal{H}(t) &= (1-s)\mathcal{H}_d + s\mathcal{H}_p \\ &= (1-s)\sum_{i=1}^N\sigma_i^x + s\left(-\frac{\hbar}{r}\sum_{i=1}^N\sigma_i^z - \frac{J}{rN}\sum_{1\leq i<j\leq N}\sigma_i^z\sigma_j^z\right) \\ &= (1-s)S_x - s\frac{\hbar}{r}S_z - \frac{sJ}{rN}(S_z)^2,\end{aligned}\quad (\text{A-1})$$

where  $S_x$  and  $S_z$  are Pauli matrices in the composite system. Considering a rotation around the  $y$ -axis by an angle  $\theta_0$ , the composite spins can be expressed as follows:

$$\begin{pmatrix} S_x \\ S_y \\ S_z \end{pmatrix} = \begin{pmatrix} -\sin\theta_0 & 0 & \cos\theta_0 \\ 0 & 1 & 0 \\ \cos\theta_0 & 0 & \sin\theta_0 \end{pmatrix} \begin{pmatrix} \tilde{S}_x \\ \tilde{S}_y \\ \tilde{S}_z \end{pmatrix}.\quad (\text{A-2})$$

Subsequently, the total Hamiltonian after  $y$ -axis rotation is written as follows:

$$\begin{aligned}\mathcal{H}(s) &= (1-s)(-\sin\theta_0\tilde{S}_x + \cos\theta_0\tilde{S}_z) \\ &\quad - s\frac{\hbar}{r}(\cos\theta_0\tilde{S}_x + \sin\theta_0\tilde{S}_z) - \frac{sJ}{rN}(\cos\theta_0\tilde{S}_x + \sin\theta_0\tilde{S}_z)^2.\end{aligned}\quad (\text{A-3})$$

After applying the Holstein–Primacoff transformation<sup>42)</sup> to Eq. (A-3), the total Hamiltonian is expressed in terms of the creation and annihilation operator  $a, a^\dagger$ . The Holstein–Primacoff transformation is given by:

$$\tilde{S}_z = \frac{N}{2} - aa^\dagger,\quad (\text{A-4})$$

$$\tilde{S}_+ = \sqrt{N - a^\dagger a} a = \sqrt{N} \sqrt{1 - \frac{a^\dagger a}{N}} a,\quad (\text{A-5})$$

$$\tilde{S}_- = a^\dagger \sqrt{N - a^\dagger a} = a^\dagger \sqrt{N} \sqrt{1 - \frac{a^\dagger a}{N}},\quad (\text{A-6})$$

$$\tilde{S}_x = \frac{1}{2} \sqrt{N - a^\dagger a} (a + a^\dagger) = \frac{\sqrt{N}}{2} \sqrt{1 - \frac{a^\dagger a}{N}} (a + a^\dagger).\quad (\text{A-7})$$

Moreover, we assume the thermodynamic limit  $N \gg \langle a^\dagger a \rangle$ . Therefore, the spin operator is represented as follows:

$$\tilde{S}_z = \frac{N}{2} - aa^\dagger,\quad (\text{A-8})$$

$$\tilde{S}_x \approx \frac{\sqrt{N}}{2} (a + a^\dagger).\quad (\text{A-9})$$

By expanding the Eq. (A-1) with spin operator after  $y$ -axis rotation, the total Hamiltonian is written as follows:

$$\begin{aligned}\mathcal{H}(s) &= \left[ -s\frac{\hbar}{r}\sin\theta_0 - (1-s)\cos\theta_0 - \frac{sJ\sin^2\theta_0}{2r} \right] \frac{N}{2} \\ &\quad - \left[ s\frac{\hbar}{r}\cos\theta_0 + (1-s)\sin\theta_0 + \right. \\ &\quad \left. + s\frac{J}{r}\cos\theta_0\sin\theta_0 \right] (a + a^\dagger) \frac{\sqrt{N}}{2} \\ &\quad + \left[ s\frac{\hbar}{r}\sin\theta_0 + (1-s)\cos\theta_0 \right] a^\dagger a\end{aligned}$$

$$\begin{aligned}
& -\frac{sJ}{4r} \cos^2 \theta_0 [a^2 + aa^\dagger + a^\dagger a + (a^\dagger)^2] + s\frac{J}{r} \sin^2 \theta_0 a^\dagger a \\
& + \frac{sJ}{2r\sqrt{N}} \cos \theta_0 \sin \theta_0 a^\dagger a (a + a^\dagger) - \frac{sJ}{rN} \sin^2 \theta_0 (a^\dagger a)^2.
\end{aligned} \tag{A-10}$$

Here, we assume that  $\frac{1}{\sqrt{N}} \rightarrow 0$ . Transforming Eq. (A-10) using the commutation relation  $aa^\dagger - a^\dagger a = 1$  yields:

$$\begin{aligned}
\mathcal{H}(s) & \approx \left[ -\frac{h}{r} \sin \theta_0 - (1-s) \cos \theta_0 - \frac{sJ \sin^2 \theta_0}{2r} \right] \frac{N}{2} \\
& - \left[ s\frac{h}{r} \cos \theta_0 + (1-s) \sin \theta_0 \right. \\
& + \left. s\frac{J}{r} \cos \theta_0 \sin \theta_0 \right] (a + a^\dagger) \frac{\sqrt{N}}{2} \\
& + \left[ s\frac{h}{r} \sin \theta_0 + (1-s) \cos \theta_0 \right. \\
& + \left. s\frac{J}{r} \sin^2 \theta_0 - \frac{sJ}{2r} \cos^2 \theta_0 \right] a^\dagger a \\
& - \frac{sJ}{4r} \cos^2 \theta_0 [a^2 + (a^\dagger)^2] - \frac{sJ}{4r} \cos^2 \theta_0.
\end{aligned} \tag{A-11}$$

Here, we define  $e, \delta$  and  $\gamma$  as

$$e \equiv \frac{1}{2} \left[ -s\frac{h}{r} \sin \theta_0 - (1-s) \cos \theta_0 - \frac{sJ \sin^2 \theta_0}{2r} \right], \tag{A-12}$$

$$\delta \equiv \left[ s\frac{h}{r} \sin \theta_0 + (1-s) \cos \theta_0 + s\frac{J}{r} \sin^2 \theta_0 - \frac{sJ}{2r} \cos^2 \theta_0 \right], \tag{A-13}$$

$$\gamma \equiv \frac{sJ}{4r} \cos^2 \theta_0. \tag{A-14}$$

We set  $\theta_0$  as  $e$  is the minimum value.

$$\frac{\partial e}{\partial \theta_0} = -s\frac{h}{r} \cos \theta_0 + (1-s) \sin \theta_0 - s\frac{J}{r} \cos \theta_0 \sin \theta_0 = 0. \tag{A-15}$$

Since calculating  $\theta_0$  that minimizes  $e$  analytically is challenging, we solve for  $\theta_0$  numerically. Following Eq. (A-12), Eq. (A-13), and Eq. (A-14), the total Hamiltonian is expressed as follows:

$$\mathcal{H}(\delta, \gamma) \approx eN + \gamma + \gamma [a^2 + (a^\dagger)^2] + \delta a^\dagger a. \tag{A-16}$$

Lastly, the Bogoliubov transformation<sup>43)</sup> is performed to  $a, a^\dagger$ .

$$a = \cosh \frac{\Theta}{2} b + \sinh \frac{\Theta}{2} b^\dagger, \tag{A-17}$$

$$a^\dagger = \cosh \frac{\Theta}{2} b^\dagger + \sinh \frac{\Theta}{2} b, \tag{A-18}$$

where,  $b, b^\dagger$  is the new creation-annihilation operator after Bogoliubov transformation. Moreover,  $\Theta$  satisfies the following equation:

$$\tanh \Theta \equiv -\frac{2\gamma}{\delta} \equiv \epsilon. \tag{A-19}$$

The total Hamiltonian after the Bogoliubov transformation is written as follows:

$$\mathcal{H}(\delta, \gamma) \approx eN + \gamma + \frac{\delta}{2} (\sqrt{1-\epsilon^2} - 1) + \Delta b^\dagger b. \tag{A-20}$$

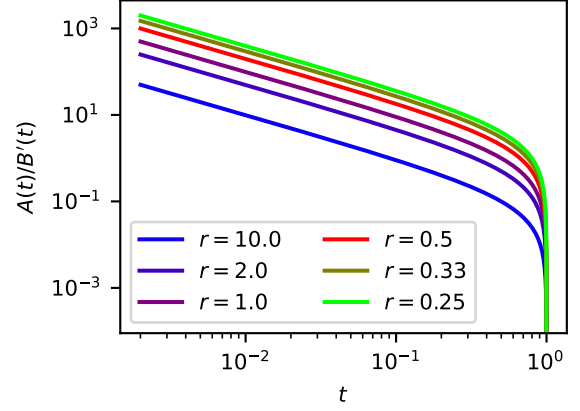


**Fig. B-1.** (Color online) Annealing schedule after fixing spins with rescaling. The vertical axis represents the ratio of the transverse local magnetic fields for the problem Hamiltonian. At  $t = 0$ , the ratio becomes infinite.

Equation (A-20) represents the Hamiltonian of the harmonic oscillator. Hence, the energy gap is expressed as follows:

$$\begin{aligned}
\Delta & = \delta \sqrt{1-\epsilon^2} \\
& = \left\{ s^2 \sin^2 \theta_0 \left( \frac{h}{r} + \frac{1 + \sin^2 \theta_0}{s \sin \theta_0} \right)^2 - \frac{(1 + \sin^2 \theta_0)^2}{s^2 \sin^2 \theta_0} \right. \\
& + \left. s^2 \sin^4 \theta_0 \frac{J^2}{r^2} + s[2 \sin^2 \theta_0 - (1-s) \cos^3 \theta_0] \frac{J}{r} \right. \\
& \left. + (1-s)^2 \cos^2 \theta_0 \right\}^{\frac{1}{2}}.
\end{aligned} \tag{A-21}$$

## Appendix B: Effective annealing schedule after rescaling

One effect of rescaling is the modification of the effective annealing schedule. By dividing the Hamiltonian by a rescaling parameter  $r$ , the effective annealing schedule is altered, as shown in Eq. (10). Consequently, the annealing schedule changes as follows:

$$\mathcal{H}'(s) = A(s)\mathcal{H}'_d + \frac{B(s)}{r}\mathcal{H}'_p, \tag{B-1}$$

$$= A(s)\mathcal{H}'_d + B'(s)\mathcal{H}'_p, \tag{B-2}$$

where  $B'(t)$  represents the effective annealing schedule after rescaling. Eq. (B-1) shows that rescaling alters only the gradient of the annealing schedule, implying that rescaling modifies the required annealing time. When the rescaling parameter is small, the crossover point, where  $A(s)/B(s) = 1$ , is delayed. Figure B-1 illustrates the changes in the annealing schedule. Numerous studies<sup>44)</sup> have highlighted the critical role of the annealing schedule in quantum annealing. Specifically, the study<sup>44)</sup> suggests that the  $k$ th derivative of the Hamiltonian at  $t = 0$  and  $t = \tau$  determines the upper bound of the excitation probability from the ground state to the first excited state. As  $r$  increases, the speed of the annealing schedule remains unaffected, as illustrated in Fig. B-1.

1) T. Kadowaki and H. Nishimori: Phys. Rev. E **58** (1998) 5355.

2) A. Finnila, M. Gomez, C. Sebenik, C. Stenson, and J. Doll: Chemical Physics Letters **219** (1994) 343.



- 3) A. Das and B. K. Chakrabarti: *Rev. Mod. Phys.* **80** (2008) 1061.
- 4) K. Tanahashi, S. Takayanagi, T. Motohashi, and S. Tanaka: *Journal of the Physical Society of Japan* **88** (2019) 061010.
- 5) B. K. Chakrabarti, H. Leschke, P. Ray, T. Shirai, and S. Tanaka: *Philosophical Transactions of the Royal Society A: Mathematical, Physical and Engineering Sciences* **381** (2023) 20210419.
- 6) S. J. Weinberg, F. Sanches, T. Ide, K. Kamiya, and R. Correll: *Sci. Rep.* **13** (2023) 4770.
- 7) B. Camino, J. Buckeridge, P. Warburton, V. Kendon, and S. Woodley: *Journal of Applied Physics* **133** (2023).
- 8) R. Honda, K. Endo, T. Kaji, Y. Suzuki, Y. Matsuda, S. Tanaka, and M. Muramatsu: *Scientific Reports* **14** (2024) 13872.
- 9) Z. Xu, W. Shang, S. Kim, E. Lee, and T. Luo: *npj Computational Materials* **11** (2025) 4.
- 10) G. Rosenberg, P. Haghnegahdar, P. Goddard, P. Carr, K. Wu, and M. L. De Prado: *Proceedings of the 8th workshop on high performance computational finance*, 2015, pp. 1–7.
- 11) E. Grant, T. S. Humble, and B. Stump: *Phys. Rev. Appl.* **15** (2021) 014012.
- 12) K. Kitai, J. Guo, S. Ju, S. Tanaka, K. Tsuda, J. Shiomi, and R. Tamura: *Phys. Rev. Res.* **2** (2020) 013319.
- 13) A. S. Koshikawa, M. Ohzeki, T. Kadowaki, and K. Tanaka: *Journal of the Physical Society of Japan* **90** (2021) 064001.
- 14) S. Izawa, K. Kitai, S. Tanaka, R. Tamura, and K. Tsuda: *Phys. Rev. Res.* **4** (2022) 023062.
- 15) T. Matsumori, M. Taki, and T. Kadowaki: *Scientific Reports* **12** (2022) 12143.
- 16) K. Nawa, T. Suzuki, K. Masuda, S. Tanaka, and Y. Miura: *Phys. Rev. Appl.* **20** (2023) 024044.
- 17) T. Inoue, Y. Seki, S. Tanaka, N. Togawa, K. Ishizaki, and S. Noda: *Opt. Express* **30** (2022) 43503.
- 18) S. Hirama and M. Ohzeki: *Journal of the Physical Society of Japan* **92** (2023) 113002.
- 19) H. Kanai, M. Yamashita, K. Tanahashi, and S. Tanaka: *IEEE Access* **12** (2024) 157669.
- 20) B. Altshuler, H. Krovi, and J. Roland: *Proceedings of the National Academy of Sciences* **107** (2010) 12446.
- 21) T. Hattori, H. Irie, T. Kadowaki, and S. Tanaka: *Journal of the Physical Society of Japan* **94** (2025) 013001.
- 22) H. Irie, H. Liang, T. Doi, S. Gongyo, and T. Hatsuda: *Sci. Rep.* **11** (2021) 8426.
- 23) H. Karimi and G. Rosenberg: *Quantum Information Processing* **16** (2017) 166.
- 24) H. Karimi, G. Rosenberg, and H. G. Katzgraber: *Phys. Rev. E* **96** (2017) 043312.
- 25) Y. Atobe, M. Tawada, and N. Togawa: *IEEE Transactions on Computers* **71** (2022) 2606.
- 26) S. Kikuchi, N. Togawa, and S. Tanaka: *Journal of the Physical Society of Japan* **92** (2023) 124002.
- 27) P. L. Hammer, P. Hansen, and B. Simeone: *Mathematical Programming* **28** (1984) 121.
- 28) V. Choi: *Quantum Information Processing* **7** (2008) 193.
- 29) V. Choi: *Quantum Information Processing* **10** (2011) 343.
- 30) W. Vinci, T. Albash, G. Paz-Silva, I. Hen, and D. A. Lidar: *Phys. Rev. A* **92** (2015) 042310.
- 31) W. Vinci, T. Albash, and D. A. Lidar: *npj Quantum Information* **2** (2016) 1.
- 32) E. Pelofske, G. Hahn, and H. N. Djidjev: *Sci. Rep.* **12** (2022) 4499.
- 33) K. Hino and S. Tanaka: *2024 IEEE International Conference on Quantum Computing and Engineering (QCE)*, Vol. 02, 2024, pp. 434–435.
- 34) M. H. Amin, A. D. King, J. Raymond, R. Harris, W. Bernoudy, A. J. Berkley, K. Boothby, A. Smirnov, F. Altomare, M. Babcock, et al.: *arXiv preprint arXiv:2311.01306* (2023).
- 35) A. Braida, S. Martiel, and I. Todinca: *npj Quantum Information* **10** (2024) 40.
- 36) A. Messiah: *Quantum Mechanics* (1976).
- 37) C. McGeoch and P. Farré: *D-Wave Technical report* (2021).
- 38) *D-Wave QPU Architecture Topologies*.
- 39) *Solver Parameters - D-Wave System Documentation*.
- 40) S. Tanaka, R. Tamura, and B. Chakrabarti: *Quantum Spin Glasses, Annealing and Computation* (Cambridge University Press, 2017).
- 41) B. Seoane and H. Nishimori: *Journal of Physics A: Mathematical and Theoretical* **45** (2012) 435301.
- 42) T. Holstein and H. Primakoff: *Phys. Rev.* **58** (1940) 1098.
- 43) N. N. Bogoljubov: *Il Nuovo Cimento (1955-1965)* **7** (1958) 794.
- 44) S. Morita: *Journal of the Physical Society of Japan* **76** (2007) 104001.